PERGAMON

Computers and Structures 80 (2002) 1651–1665

Computers & Structures

www.elsevier.com/locate/compstruc

Simulating cyclic artery compression using a 3D unsteady model with fluid–structure interactions

Dalin Tang [a,*], Chun Yang [b], Homer Walker [a], Shunichi Kobayashi [c], David N. Ku [d]

[a] *Mathematical Sciences Department, Worcester Polytechnic Institute, 100 Institute Road, Worcester, MA 01609-2280, USA*
[b] *Mathematics Department, Beijing Normal University, Beijing, China 100875*
[c] *Department of Functional Machinery and Mechanics, Shinshu University, 3-15-1 Tokida Ueda, 386-8567 Nagano, Japan*
[d] *Georgia Institute of Technology, School of Mechanical Engineering, Atlanta, GA 30322, USA*

Received 11 October 2001; accepted 24 April 2002

Abstract

High pulsating blood pressure and severe stenosis make fluid–structure interaction (FSI) an important role in simulating blood flow in stenotic arteries. A three-dimensional nonlinear model with FSI and a numerical method using GFD are introduced to study unsteady viscous flow in stenotic tubes with cyclic wall collapse simulating blood flow in stenotic carotid arteries. The Navier–Stokes equations are used as the governing equations for the fluid. A thin-shell model is used for the tube wall. Interaction between fluid and tube wall is treated by an incremental boundary iteration method. Elastic properties of the tube wall are determined experimentally using a polyvinyl alcohol hydrogel artery stenosis model. Cyclic tube compression and collapse, negative pressure and high shear stress at the throat of the stenosis, flow recirculation and low shear stress just distal to the stenoses were observed under physiological conditions. These critical flow and mechanical conditions may be related to platelet aggregation, thrombus formation, excessive artery fatigue and possible plaque cap rupture. Computational and experimental results are compared and reasonable agreement is found.

Keywords: Generalized finite difference; Free moving boundary; Stenosis; Blood flow; Artery

1. Introduction

A nonlinear three-dimensional (3D) model with fluid–structure interactions (FSI) and an iterative numerical method based on generalized finite difference (GFD) are introduced to model unsteady blood flow in stenotic arteries and simulate cyclic wall compression and unsteady viscous flow in a stenotic elastic tube with large strain and large deformation. Flow velocity accelerates when passing through a stenosis (a constriction in blood vessels) which lowers flow pressure. If the stenosis is severe enough, blood pressure may become negative and cause artery compression or even collapse leading to serious clinical consequences such as stroke or heart attack [1,3,41,44]. The mechanism for the whole collapse process is not fully understood. Since blood flow is pulsatile and tube collapse is fully 3D, a 3D unsteady model is necessary even though the resting shape of the stenotic tube is axisymmetric in this simulation. The incompressible Navier–Stokes (N–S) equations are used for the fluid model while a thin-shell model is used for the tube wall so that cyclic wall collapse can be simulated [10]. Pressure–cross-section area relationship of the tube wall (known as the tube law, which is essentially a bi-axial stress/strain relation) is

* Corresponding author. Tel.: +1-508-831-5332; fax: +1-508-831-5824.
E-mail address: dtang@wpi.edu (D. Tang).

0045-7949/02/$ - see front matter
PII: S0045-7949(02)00111-6

measured at three locations of the tube experimentally using a PVA hydrogel stenotic tube whose mechanical properties are close to that of bovine carotid arteries [23,24]. The classic tube law introduced for a uniform collapsible tube [21,38] is extended to include axial position, longitudinal tension and axial curvature changes so that it is more suitable for a stenotic compliant tube. A physiological 36.5% axial pre-stretch is applied to the stenotic tube model. Physical parameters and geometrical dimensions corresponding to blood flow in human carotid arteries are used to make the model physiologically relevant. In the computational wall model, tube expansion (which is not assumed to be axisymmetric) under positive pressure is obtained pointwisely using a pressure–radius relationship derived from the tube law. For tube deformation under negative pressure, the circumferential arc length is assumed to be inextensible [10], and tube compression and collapse are determined by solving the thin-shell equilibrium equations using flow pressure and shear stress distributions on the tube wall. Mechanical parameters such as the Young's modulus and the bending stiffness coefficient are determined by experimental measurements. The wall model and fluid model are solved iteratively using an incremental boundary iteration method [37]. Effects of stenosis severity and pressure conditions on cyclic wall bending and compression, flow velocity, pressure, and shear stress are investigated to quantify possible wall collapse conditions and flow characteristics which may be related to artery fatigue and plaque cap rupture. Details of the model, method and results are given in the following sections.

2. Background

FSI play important roles in many biological processes, especially for blood flow in stenotic arteries. Blood vessels are highly compliant. Under pulsatile blood pressure, high grade stenoses cause critical flow and mechanical conditions such as high flow velocity, high shear stress, flow recirculation, negative pressure and cyclic artery compression which may be related to platelet aggregation, thrombus formation, and excessive artery fatigue (for reviews, see [25,47]). Changes in blood pressure causes artery deformation which affects stenosis severity (percentage of artery diameter narrowing). A small change in stenosis severity leads to considerable changes of flow velocity, shear stress and pressure in the stenotic region, which in turn affects artery deformation. The FSI continues and may lead to artery compression or even collapse when stenosis becomes severe enough (severity 70–80% in diameter). There has been increasing evidence that stenotic plaque may rupture under physiological conditions and cause fatal subsequential atherosclerotic diseases such as myocardial infarction, cerebral stroke, etc. [5,7,8,15,30]. Experiment-based computational models with strong FSI are needed to better understand these processes and to quantify physiological conditions under which artery collapse may occur.

Extensive experimental research have been conducted to quantify mechanical properties of arteries [13,14,18]. However, most of the data obtained are for arteries under expansion with positive pressures. For collapsible tubes, pressure–tube cross-section area relationship (tube law) has been widely used to describe the elastic properties of the tube wall under both positive and negative pressure conditions. Considerable work for flow in collapsible tubes of uniform diameter has been reported in the last 25 years and many interesting phenomena such as flow choking, flow limitation and dynamic behavior (flutter) have been identified and investigated (for a review, see [9,32]). For flow in stenotic collapsible tubes and arteries, research has been focused on the effect of stenosis severities on the flow and wall motions under various pressure conditions. Different stenoses were used in several investigations to quantify pressure–area and pressure–flow relations and collapse conditions [4,20,23,24,34,39,41].

Various computational models (from 1D to 3D, with rigid or compliant tubes) have been used to quantify flow and wall mechanical behaviors [1,3,9,11,21,27, 44,48]. It has been found that artery stiffness, stenosis geometry and severity and imposed pressure conditions are the dominating factors affecting blood flow and artery motion. However, except the 1D models, higher dimensional models with FSI simulating cyclic wall compression and collapse are still lacking in the literature for the following reasons:

(i) Mechanical properties of arteries under compression are not readily available. Without the experimental data, modeling for artery compression will have no supporting basis and no validation.
(ii) Stenotic artery wall behavior under pulsatile pressure is very complex. It is fully 3D, dynamic, involves large strain, large deformation, and cyclic tube collapse and expansion. Severe stenosis makes FSI very strong with small change in one causing large change in another. Regular boundary iteration methods may fail to converge because of that [37].
(iii) Severe stenosis causes critical flow conditions which are computationally difficult to handle. Algorithms that converge for normal pressure and flow conditions may not converge under these critical conditions. For the case we are considering, flow pressure drops from 150 to −12.5 mmHg just across a 80% stenosis. That is from about 199,800 to −16,650 dyn/cm^2 in less than 1 cm. That leads to very large pressure gradient (10^5) in the flow field. The flow speed at the throat of the stenosis is about

400 cm/s just 0.01 cm away from the wall which leads to very high flow shear stress on the tube wall. These critical conditions require special handling, at least much finer mesh should be used near the tube wall and stenosis to get enough resolution.

The above leads to the introduction of our computational model which provides a first order approximation of the complex artery cyclic collapse process with available experimental data.

3. The Computational model

3.1. The fluid model

We consider viscous flow in a compliant tube simulating pulsatile blood flow in stenotic carotid arteries. The flow is assumed to be laminar, Newtonian, viscous and incompressible. Using the arbitrary Lagrangian–Eulerian (ALE) formulation [19,35], the N–S equations become:

$$\rho(\partial\mathbf{u}/\partial t + ((\mathbf{u}-\mathbf{u}_g)\cdot\nabla)\mathbf{u}) = -\nabla p + \mu\nabla^2\mathbf{u}, \tag{1}$$

$$\nabla\cdot\mathbf{u} = 0, \tag{2}$$

where $\mathbf{u}$ and p are flow velocity and pressure, $\partial/\partial t$ is t-derivative with mesh points fixed, $\mathbf{u}_g$ is the mesh velocity. Assuming the fluid and wall move together at the tube wall, we have:

$$\mathbf{u} = (u,v,w)|_\Gamma = \frac{\partial\mathbf{x}}{\partial t}. \tag{3}$$

Here Γ stands for the inner tube wall (Fig. 1), $\mathbf{x} = (r,\theta,z)$ is the position vectors of the deformed tube wall, u, v and w are the radial, angular and axial components of the flow velocity. The undeformed inner tube wall radius with a symmetric stenosis is given by

$$R(Z) = R_0 - S(Z), \tag{4}$$

$$S(Z) = \begin{cases} S_0R_0\dfrac{\left[1-\cos\left(\dfrac{2\pi(Z-Z_1)}{(Z_2-Z_1)}\right)\right]^2}{4}, & Z_1 \leqslant Z \leqslant Z_2, \\ 0, & \text{otherwise.} \end{cases} \tag{5}$$

where $\mathbf{X} = (R,\Theta,Z)$ is the position vector of the undeformed tube wall, R_0 is the radius of the uniform part of the tube, $S(Z)$ specifies the shape of the stenosis, S_0 is the stenosis severity by diameter, i.e., reduction of the tube diameter caused by the stenosis, Z_1 and Z_2 specify the beginning and ending of the stenosis. Stenosis severity is commonly defined as

$$S_0 = \frac{(R_0 - R_{\min})}{R_0}\times 100\%. \tag{6}$$

At the inlet and outlet of the tube, we set:

$$p|_{z=0} = p_{\text{in}}(t), \quad p|_{z=\ell} = p_{\text{out}}(t), \tag{7}$$

$$\left.\frac{\partial\mathbf{u}}{\partial z}\right|_{z=0,\ell} = 0. \tag{8}$$

We start the computation from zero pressure and zero flow state and gradually raise the pressure to the prescribed conditions.

3.2. The wall model

Mechanical properties of arteries under compression and pulsatile conditions are very hard to obtain. It is hard to simulate dynamic wall deformation and collapse correctly without this information. However, to measure the 3D nonlinear dynamic wall mechanical properties and solve the complete nonlinear wall model [13] involving large strain and large deformation in the collapse process is a forbidding task. Most existing linear or nonlinear wall models for arteries are applicable only to normal positive pressure conditions and are no longer valid when pressure becomes negative and the artery is under compression [13,40].

In this paper, we use tube law and a thin-shell model [10] to determine the wall motion under both positive and negative pressure conditions. To determine the elastic properties of the stenotic tube, the pressure–area relationship (tube law)

$$(p-p_e)|_{Z=Z_i} = p_i(\alpha), \quad \alpha = A/A_0, \ \ i = 1,2,3 \tag{9}$$

is measured for a tube made of PVA hydrogel with a 80% thick-walled stenosis under 36.5% axial stretch. The measurements are taken at three locations of the tube (straight, shoulder and throat) to take the stenotic effect into consideration. The experimental data is given by Fig. 1. A and A_0 are the deformed and undeformed cross-section areas of the tube respectively. The external pressure p_e is set to zero in this paper. For computational convenience (as well as when conducting the experiments), the inverse of (9) is used to determine α when p is given (noting $p_e = 0$),

$$\alpha = \alpha_i(p), \quad i = 1,2,3. \tag{10}$$

Mathematical interpolation is used to connect the three experimentally measured tube laws to cover the entire tube

$$\alpha_g(z,p) = \sum_i C_i(z)\alpha_i(p), \quad \alpha_g(z_i,p) = \alpha_i(p), \tag{11}$$

where $C_i(z)$ are properly chosen to reflect the influence of the shape and stiffness of the stenosis.

Wall deformation is determined using two different methods depending on whether the tube is under expansion or compression. For the portion where the

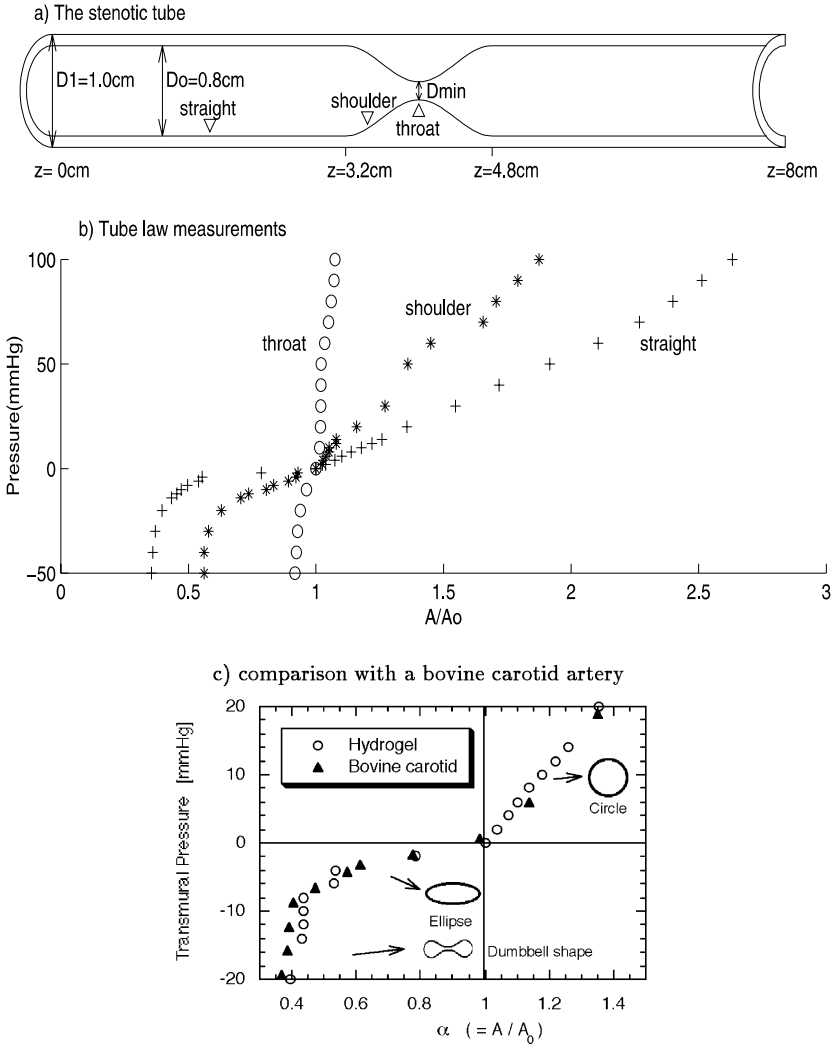

Fig. 1. The stenotic tube and the tube law measurements.

pressure is positive, the tube is under expansion and axisymmetric (or is nearly axisymmetric), (11) is used to derive the radius–pressure relation:

$$r = r(z, p). \tag{12}$$

which is used to determine tube radius pointwisely. Eq. (12) is equivalent to a stress/strain relation for the tube under positive pressure conditions.

For the post-buckling stage, tube law (11) is no longer adequate to determine the tube deformation because the tube is no longer nearly axisymmetric. Actually, for $\alpha < 1$, our experimental measurements provide additional information for tube wall deformation under compression (see Fig. 1 for collapsed shape). We use a thin-shell model [10] to determine wall deformation under compressed or collapsed conditions. Motivated by Peskin's fiber idea [33], we discretize the tube wall by a set of z-rings and a set of θ-lines (longitudinal lines on the tube with fixed θ angles). Following Flaherty [10], the rings are assumed to be inextensible (so it will change shape under negative pressure or stress) and the bending moment M is assumed to be proportional to the curvature change:

$$M = K_{\mathrm{p}}(1/R - \kappa_{\mathrm{c}}), \tag{13}$$

where R is the undeformed tube radius, κ_{c} is the deformed ring curvature, and K_{p} is a stiffness coefficient determined by the wall material and geometry. For a thin-wall tube, K_{p} is determined by [9]:

$$K_{\mathrm{p}} = \frac{E h_{\mathrm{w}}^3}{12(1-\nu^2)r^3}, \tag{14}$$

where E is the Young's modulus of the tube determined from experiment [44], h_{w} is wall thickness, ν is Poisson

ratio, r is the mean tube radius. Following the derivation in Flaherty's paper [10] with some adjustments, use the natural coordinates and neglecting the inertia force (<1% of tension forces) and the circumferential shear stress from the fluid, the equilibrium equations for the tube wall are given by

$$\frac{\partial T_c}{\partial s_1} + \kappa_c N = 0, \tag{15}$$

$$\frac{\partial N}{\partial s_1} - \kappa_c T_c = -(p + K_p T_L(\kappa_L - \kappa_{L0}))\cos\beta, \tag{16}$$

$$\frac{\partial M}{\partial s_1} + N = 0, \tag{17}$$

$$\frac{\partial T_L}{\partial s_2} = -\tau, \tag{18}$$

where T_c and N are the tangential and outward normal components of the resultant stress on the z-rings respectively, T_L is the longitudinal tension along the θ-lines and τ is the fluid shear stress, κ_L and κ_{L0} are curvatures of the deformed and undeformed θ-lines, β is the angle between the normal directions of the ring and the tube wall surface, s_1 and s_2 are the arc lengths along the z-rings and θ-lines respectively. The axial tension and strain relationship is measured experimentally,

$$\epsilon_L = \epsilon_L(T_L), \tag{19}$$

which is needed to determine the axial displacement of the grid points when T_L is obtained from (18). The inlet and outlet of the tube are not allowed to move in the axial direction to prevent the entire tube from being pushed away by the flow. This completes the FSI model.

Remark 1. Due to lack of information about the constitutive laws of arteries under compression, the thin-shell model and tube law (11) combined together provide a direct method to determine tube deformation under collapsed condition. While the wall model is very simplified, the wall deformation obtained is controlled directly by experimental data, and the results obtained provide a good approximation for wall and flow behaviors in the physiological artery collapse process. Better wall models and experimental data for tube material under compression are needed to get detailed stress/strain distributions in the tube wall which cannot be obtained from the current model [43,44].

4. The numerical method

A numerical method using the conventional ALE-based staggered GFD over an irregular grid with upwind differencing and an incremental boundary iteration technique for FSI is introduced to solve the model [19,22,29,31,37]. Use of ALE formulation enables us to choose the mesh properly to avoid large mesh distortion and eliminates the needs of interpolating the flow variables for previous steps at the new grids. GFD makes it possible for us to use finer mesh near the tube wall and in the stenotic region to handle the critical flow conditions involved in the problem (Fig. 2). The incremental boundary iteration method is essentially a relaxation technique which is used to handle "pressure over-shooting" and "boundary over-shooting" [2,37] and improve on the regular boundary iteration method to get convergence for the FSI model with large strain and large deformations. Details of the numerical method are outlined below.

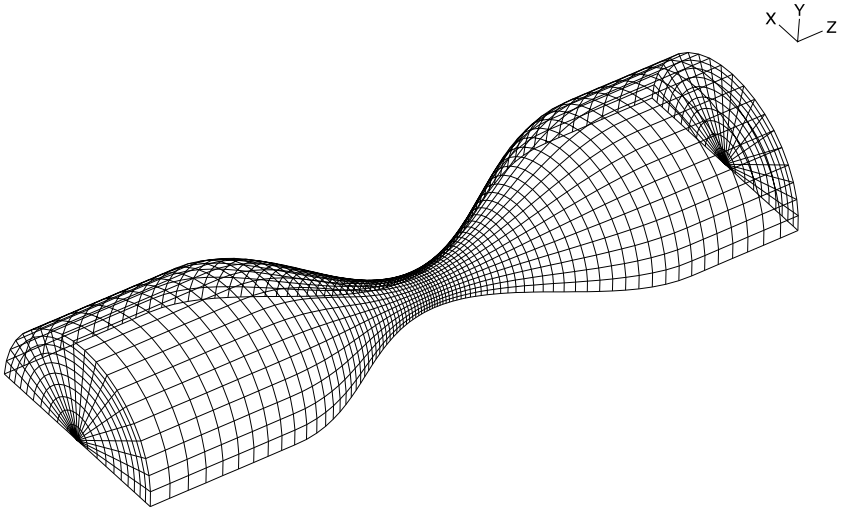

Fig. 2. The nonuniform mesh used in the computation.

4.1. The generalized finite difference concept

The advantage of the GFD method is that GFD schemes can be derived using arbitrary irregular grids [29]. To derive the second order GFD schemes for the derivatives $f_r, f_\theta, f_z, f_{rr}, \ldots, f_{zz}$ at a given point $\mathbf{x}_0$, let $\mathbf{x}_i(r_i, \theta_i, z_i)$, $(i = 1, \ldots, n,\ n \geqslant 9)$ be n neighboring points of $\mathbf{x}_0$ and,

$$a_i = r_i - r_0, \quad b_i = \theta_i - \theta_0, \quad c_i = z_i - z_0,$$
$$\rho_i = [a_i^2 + b_i^2 + c_i^2]^{1/2}, \quad f_i = f(r_i, \theta_i, z_i),$$

use the Taylor expansion of f at $\mathbf{x}_0$ and omitting higher order terms, we have,

$$f_i = f_0 + a_i f_r^0 + b_i f_\theta^0 + c_i f_z^0 + \tfrac{1}{2}(a_i^2 f_{rr}^0 + b_i^2 f_{\theta\theta}^0 + c_i^2 f_{zz}^0 + 2a_i b_i f_{r\theta}^0 + 2b_i c_i f_{\theta z}^0 + 2a_i c_i f_{rz}^0). \tag{20}$$

The GFD schemes for the nine derivatives can be obtained from these equations using least-squares approximations with proper weight functions. Other GFD schemes can be derived similarly. Because there are virtually no restrictions on the selection of the points $\mathbf{x}_i$ and the GFD schemes can be obtained automatically in the computer program each time the domain and mesh are adjusted, the GFD method is a suitable tool to handle the irregular geometry with nonuniform grids and a free moving boundary which requires frequent remeshing of the domain.

4.2. Discretization of N–S equations over the irregular geometry with a nonuniform mesh

Rewriting the N–S equations into the form (use the u-equation as an example),

$$\rho u_t + \left(\rho(u - u_g), \frac{\rho(v - v_g)}{r}, \rho(w - w_g)\right)(u_r, u_\theta, u_z)^T + p_r + \left(-\frac{\mu}{r}, 0, 0, -\mu, -\frac{\mu}{r^2}, -\mu\right)(u_r, u_\theta, u_z, u_{rr}, u_{\theta\theta}, u_{zz})^T - \frac{\rho}{r}v^2 - \frac{\mu u}{r^2} + \frac{2\mu}{r^2}v_\theta = 0, \tag{21}$$

for each grid point $\mathbf{x}_0$, using a three-point backward difference scheme $u_t \approx (3u^{(n+1)} - 4u^n + u^{(n-1)})/2\Delta t$ for the t-derivative, (u, v, w) values from last iteration in the convection terms to linearize the equation, the GFD schemes for the space derivatives with the neighboring points with staggered grids and upwind techniques (Fig. 3), and rearranging the terms and omitting the superscript $(n + 1)$, we have the discretized equation:

$$u_0 + \sum_{i=1}^{18} k_i^u u_i + k_{19}^u + \sum_{i=1}^{18} k_{19+i}^u p_i = 0,$$

where the nonhomogeneous term k_{19}^u came from quantities considered known at this step. The other equations

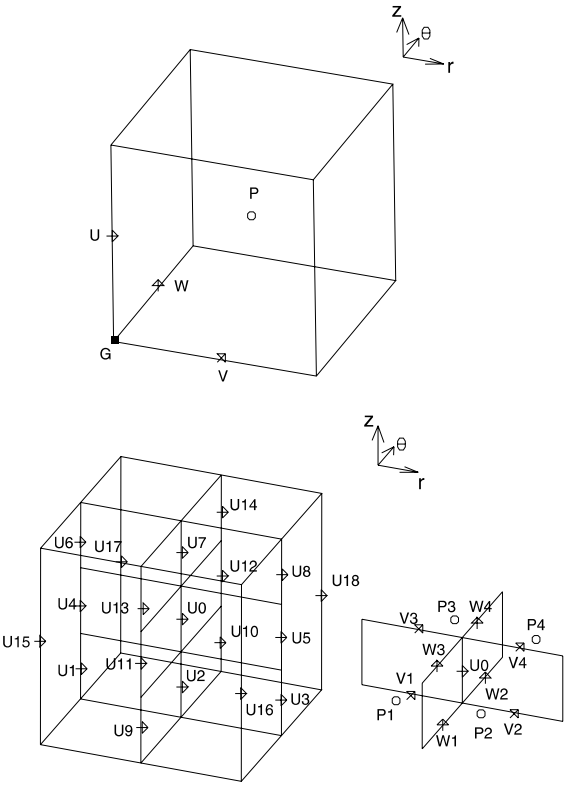

Fig. 3. The staggered grids and numbering of the neighboring points.

can be discretized in the same way. Using vector notation, we have:

$$\mathbf{u}_0 + \sum_{i=1}^{18} k_i^{\mathbf{u}} \mathbf{u}_i + k_{19}^{\mathbf{u}} + \sum_{i=1}^{18} k_{19+i}^{\mathbf{u}} p_i = 0, \quad \text{(equation of motion)} \tag{22}$$

$$\sum_{i=1}^{12} k_i^c u_i + \sum_{i=1}^{12} k_{12+i}^c v_i + \sum_{i=1}^{12} k_{24+i}^c w_i + k_{37}^c = 0, \quad \text{(equation of continuity)} \tag{23}$$

where notations $k_i^{\mathbf{u}} = (k_i^u, k_i^v, k_i^w)^T$ and $k_i^{\mathbf{u}}\mathbf{u}_i = (k_i^u u_i, k_i^v v_i, k_i^w w_i)^T$ were used for simplicity.

4.3. The SIMPLER algorithm

Because the fluid–wall interaction model is complex, we start from a well-tested SIMPLER algorithm [31] to solve (22) and (23). Let the residuals of the equations of motion by $\mathbf{u}^m$, p^m be:

$$\mathbf{u}_0^m + \sum_{i=1}^{18} k_i^{\mathbf{u}} \mathbf{u}_i^m + k_{19}^{\mathbf{u}} + \sum_{i=1}^{18} k_{19+i}^{\mathbf{u}} p_i^m = \mathbf{R}_{\mathbf{u}}(\mathbf{u}^m, p^m), \tag{24}$$

where notations $k_i^{\mathbf{u}}$, $k_i^{\mathbf{u}}\mathbf{u}_i^{\mathrm{m}}$ and $\mathbf{R}_{\mathbf{u}}$ were used in a similar way as before. Assuming $\mathbf{u}^{\mathrm{m}}+\delta\mathbf{u}$ and $p^{\mathrm{m}}+\delta p$ satisfy (22) and using (24) and (22) becomes,

$$(\delta\mathbf{u})_0+\sum_{i=1}^{18}k_i^{\mathbf{u}}\delta\mathbf{u}_i+\sum_{i=1}^{18}k_{19+i}^{\mathbf{u}}\delta p_i+\mathbf{R}_{\mathbf{u}}(\mathbf{u}^{\mathrm{m}},p^{\mathrm{m}})=0,$$

neglecting $\delta\mathbf{u}_i$ terms leads to:

$$(\delta\mathbf{u})_0=-\sum_{i=1}^{18}k_{19+i}^{\mathbf{u}}\delta p_i-\mathbf{R}_{\mathbf{u}}(\mathbf{u}^{\mathrm{m}},p^{\mathrm{m}}). \tag{25}$$

Substituting $\mathbf{u}^{\mathrm{m}}+\delta\mathbf{u}$ into (23) and using (25), δp can be determined. Then $\delta\mathbf{u}$ follows from (25) and $\mathbf{u}$ and p can be updated accordingly.

4.4. Incremental boundary iteration method

Boundary iteration methods have become popular for solving problems with FSI recently where the fluid and solid models are solved iteratively until convergence is obtained. However, it has been known that the boundary iteration method may fail to converge if the tube wall is considerably compliant [37]. We use an incremental iterative method to reduce the "displacement over-shooting" and improve the convergence. Displacement over-shooting causes velocity over-adjustment at the boundary which affects the convergence of the fluid model. For a given wall adjustment $\Delta r(\theta,z)$, if the fluid model fails to converge, we reduce Δr to half and try to solve the fluid model again. This is repeated until convergence is reached. A similar relaxation technique can also be used to reduce "pressure over-shooting" which is the cause of tube wall over-adjustment. When $\delta\mathbf{u}$ and δp are obtained, we update $\mathbf{u}$ and p with

$$\mathbf{u}_{\mathrm{new}}=\mathbf{u}_{\mathrm{old}}+\omega_u\delta\mathbf{u},\quad p_{\mathrm{new}}=p_{\mathrm{old}}+\omega_p\delta p, \tag{26}$$

where ω_u and ω_p can be chosen between 0 and 1 to achieve best convergence.

4.5. Numerical method for the wall model

We introduce an iterative method to solve the thin-shell model. At each boundary iteration, the material coefficients are determined for each grid point with updated pressure information using the tube laws. Then Eqs. (15)–(17) are solved on each ring with updated pressure and longitudinal tension to determine the circumferential and radial displacements [10]. With these adjustments, (18) is solved to update the longitudinal tension which determines the axial displacement of each grid point. Then (15)–(17) are solved again. This is repeated until convergence is reached.

5. Results

Computations are conducted for various pressure and stenosis conditions to quantify cyclic wall compression and collapse phenomena and related flow behaviors. Inlet (upstream) pressure is set to 70–110 mmHg and 90–150 mmHg respectively representing normal and high blood pressures. As for the distal pressure, Hafner has reported a carotid stump pressure between 0 and 25 mmHg for 78 out of 418 patients [17]. So outlet (downstream) pressure is set to 20, 10 or 0 mmHg for different cases in our computations and experiments. Cyclic wall compression, tube collapse and flow characteristics for an 80% stenosis (by diameter) with $p_{\mathrm{in}}=90$–150 mmHg and $p_{\mathrm{out}}=20$ mmHg are more critical and results are presented in more details. Results of other cases are reported as appropriate.

5.1. Parameters, geometry, mesh and convergence

The ranges of parameters and the geometry of the tube used in the computations are chosen to match the experimental set-up [23,26]:

$$R_0=0.4\text{ cm},\ l=8\text{ cm (tube length)},\ Z_1=3.2\text{ cm},$$
$$Z_2=4.8\text{ cm},\ \nu=0.04\text{ cm}^2/\text{s},\ \rho=1\text{ g/cm}^3,\ \nu=\mu/\rho.$$

Reynolds number Re is defined as $D\cdot U/\nu$ where D is the entrance tube diameter ($2R_0$) and U is the entrance average velocity. The Reynolds number for a 80% stenosis with inlet pressure 100 mmHg and outlet pressure 20 mmHg is about 300. The units given above are used throughout the paper.

Nonuniform meshes (Fig. 2) are used in the computation to handle the critical flow conditions involved in the collapse process. We look for solutions which are symmetric with respect to the horizontal plane and the model is solved over the (r,θ,z)-domain $[0,H]\times[0,\pi]\times[0,l]$. The step sizes in r- and z-directions are reduced by fixed ratios towards the wall and the middle of the tube length to get better resolution there. The ratios are

$$q_r=\frac{\mathrm{d}r_{i+1}}{\mathrm{d}r_i}=0.92,\quad q_z=\frac{\mathrm{d}z_{i+1}}{\mathrm{d}z_i}=0.95. \tag{27}$$

For a $(10_r\times20_\theta\times120_z)$ mesh, we have $\mathrm{d}r_1=0.0566$, $\mathrm{d}r_{10}=0.0267$ at the inlet of the tube where the step size at the wall $\mathrm{d}r_{10}$ is less than half of the starting step size $\mathrm{d}r_1$. For z, we have $\mathrm{d}z_1=0.2097$ at the inlet, $\mathrm{d}z_{60}=0.01017$ at the middle of the tube length which is about 1/20 of $\mathrm{d}z_1$. Uniform step size is used for θ variable. By using nonuniform mesh, much better resolution is achieved near the wall and stenotic region with fewer grid points which lead to considerable savings of memory and CPU time.

Since analytic solutions for flow in a compliant stenotic tube are not available, numerical solutions are

compared with the exact solution for flow in a rigid straight tube [12],

$$w = -\frac{1}{4v}(R_0^2 - r^2)p_z, \quad u = v = 0, \quad p_z = (p_{\text{out}} - p_{\text{in}})/l. \tag{28}$$

and Table 1 gives a summary of the errors which show that the algorithm converges reasonably well. The accuracy of the numerical solutions may be better than what Table 1 shows because the exact solution is assumed to be z-independent while the actual tube length is always finite and the numerical solutions are slightly z-dependent.

To check the accuracy and convergence of the algorithm for the complaint model with stenosis, three meshes were tested and the results are given in Table 2. As the mesh gets finer, errors decrease roughly in a linear fashion indicating that the method is of first-order accuracy. Mesh $(10_r \times 20_\theta \times 120_z)$ is used in our general computations in this paper. The tolerance for the N–S solver (SIMPLER iteration) is set to 1.0×10^{-7}, i.e. solutions of (22) and (23) are considered obtained if the relative errors (corrections) of velocity and pressure are less than the specified tolerance (TOL1). The tolerance for the boundary iteration is set to 1.0×10^{-4} (TOL2), i.e., the solution for the tube wall, flow velocity and pressure were considered ''converged'' for a given time step if the relative errors became less than the tolerance specified. Periodic solutions were considered obtained when the solutions started to repeat itself within 1% tolerance (TOL3). Our calculations indicate that three periods are needed for the solutions to become periodic.

5.2. Wall deformation, cyclic wall compression and collapse

Fig. 4 shows tube deformation when the inlet pressure is at its minimum and maximum respectively. The tube is collapsed at the distal side of the stenosis when inlet pressure is at its maximum. The location of the collapse is about one diameter distal to the stenosis, consistent with experimental observations. The cyclic compression repeats as the inlet pressure changes periodically.

Fig. 5 gives ultrasound images of the vertical views of the tube with pressure conditions set at $p_{\text{in}} = 70$–130 mmHg and $p_{\text{out-avg}} = 0$ mmHg. The tube is fully collapsed when p_{in} is at its maximum. $p_{\text{out-avg}}$ was set to 0 mmHg in the experiment so that full tube collapse could be observed. $p_{\text{out}} = 20$ mmHg is more physiologically relevant and is used in our numerical simulation as the main case.

5.3. Negative pressure in the stenotic tube

Pressure imposed at inlet is given by Fig. 6(a). Since pressure is directly related to tube compression and collapse, minimum pressure for the entire fluid domain as a function of time is plotted in Fig. 6(b). The slight waviness is due to the fact that minimum pressure may occur at different neighboring points for different times. Transmural pressure at the tube wall at $t = 0.5$ is plotted in Fig. 6(c). Transmural pressure at the tube wall at $\theta = 90°$ changing with time is plotted by Fig. 7. Pressure distributions inside the tube were reported in our pre-

Table 1
Comparison of 3D numerical solutions with exact solution for flow in a rigid straight tube[a]

$r \times \theta \times z$	$e_n(u)$	$e_n(v)$	$e_n(w)$	$e_n(p)$
$20 \times 16 \times 60$	5.7×10^{-7}	4.4×10^{-9}	0.098	3.7×10^{-6}
$30 \times 20 \times 80$	3.1×10^{-7}	4.2×10^{-9}	0.031	2.3×10^{-6}
$40 \times 24 \times 100$	1.4×10^{-7}	3.8×10^{-9}	0.018	1.1×10^{-6}

[a] $p_{\text{in}} = 100$ mmHg, $p_2 = 99.8$ mmHg, $u_{\max}$ (exact) $= 32.98$ cm/s, $\mathrm{d}t = 0.005$, time step computed $= 1600$. Relative errors are defined as $e_n(f) = \|f_n - f_{\text{exact}}\|_2 / \|f_n\|_2$, n = time step.

Table 2
Order of accuracy of the numerical method[a]

$r \times \theta \times z$	$(\mathrm{d}r, \mathrm{d}\theta, \mathrm{d}z)_{\text{end}}$	$e_n(u)$	$e_n(v)$	$e_n(w)$	$e_n(p)$	$e_n(H)$
$8 \times 16 \times 80$	(0.0367, 0.196, 0.0310)	3.918E−3	1.283E−10	1.369E−3	9.922E−6	4.683E−6
$10 \times 20 \times 100$	(0.0267, 0.157, 0.0175)	2.398E−3	1.343E−11	0.874E−3	5.981E−6	2.584E−6
$12 \times 24 \times 120$	(0.0202, 0.131, 0.0102)	1.527E−3	2.473E−12	0.538E−3	3.791E−6	1.576E−6

[a] $p_1 = 130$ mmHg, $p_2 = 40$ mmHg, $S_0 = 80\%$, $\mathrm{d}t = 0.001$, time steps computed $= 800$. Mesh step size reduction ratios are 0.92 for r and 0.95 for z. Step sizes given in the table are the minimum r-step size at the inlet of the tube and the minimum z-step at the middle of the tube length.

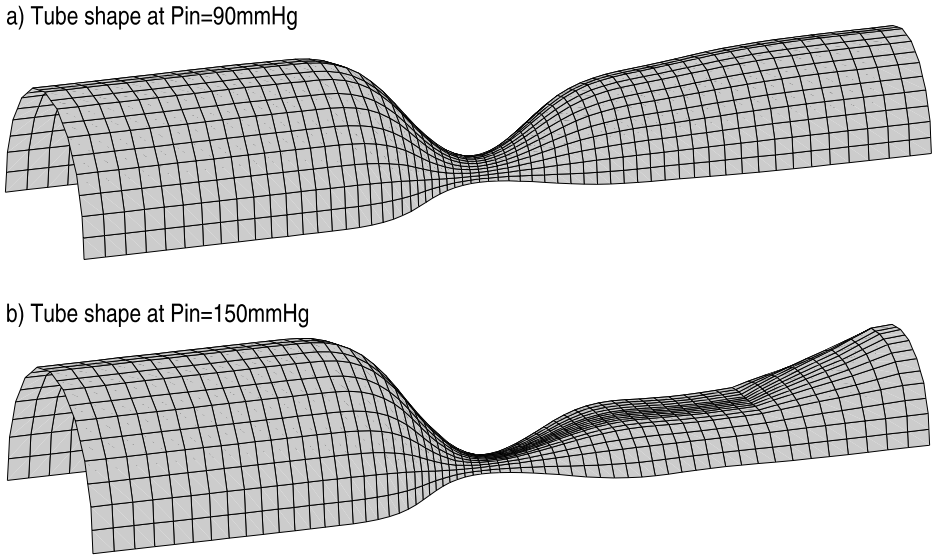

Fig. 4. Numerical results for tube wall deformation under maximum and minimum inlet pressure showing cyclic wall compression. $p_{in} = 90$–150 mmHg, $p_{out} = 20$ mmHg, $S_0 = 80\%$, portion of the tube plotted: $z = 1.5$–6.5 cm.

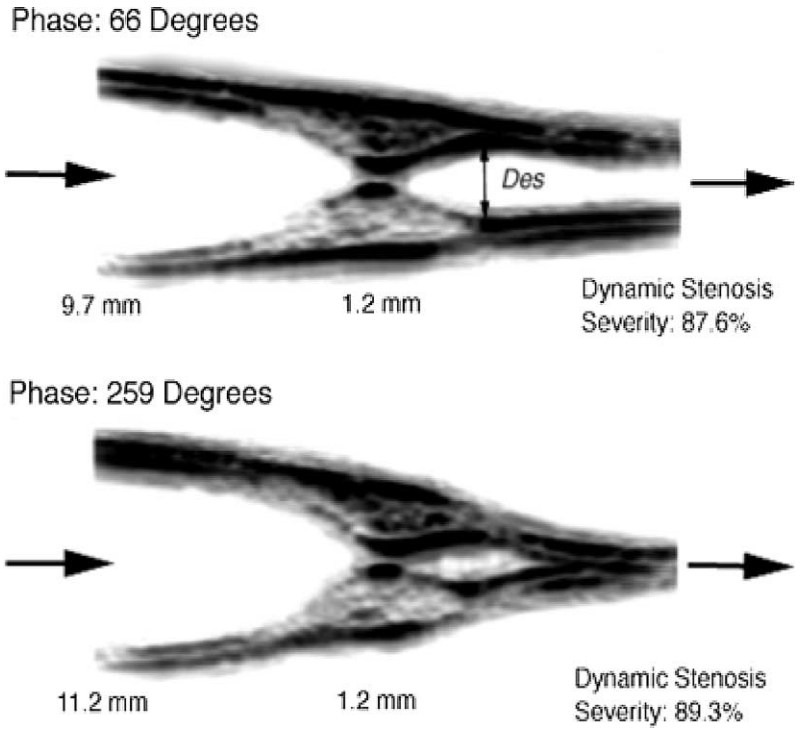

Fig. 5. Ultrasound image of cross-section during flow collapse. $p_{in} = 70$–130 mmHg, $p_{out\text{-}avg} = 0$ mmHg.

vious papers [45,46] and it was found that minimum pressure occurs at the throat of stenosis. Because the prescribed inlet and outlet pressures are positive, the pressure inside the tube is, in general, positive and the tube is inflated almost everywhere (about 60% at the inlet under 100 mmHg). However, negative pressure may occur at and distal to the stenosis if the stenosis is severe enough and pressure drop is large enough. Minimum pressure occurs at the throat of the stenosis as expected. Fig. 6(c) and Fig. 7 show clearly that the

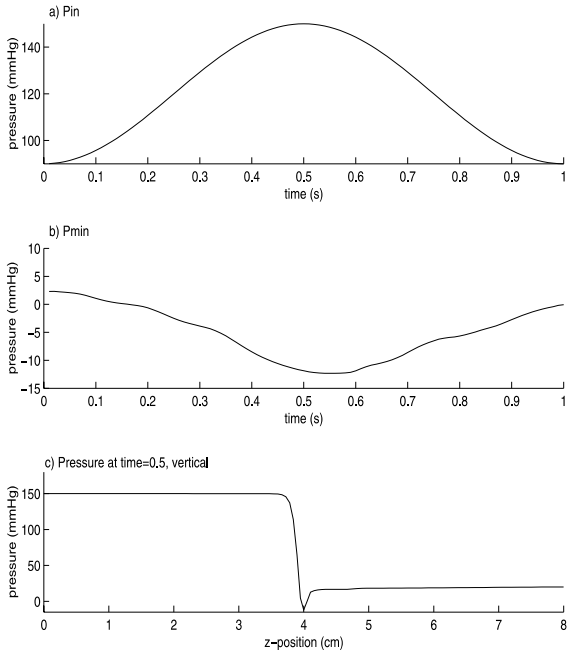

Fig. 6. Transmural pressure changes drastically across the stenosis: (a) the inlet pressure; (b) minima of the corresponding pressure field; (c) transmural pressure at $t = 0.5$ s along the tube wall. $p_{in} = 90$–150 mmHg, $p_{out} = 20$ mmHg, $S_0 = 80\%$.

pressure does not change much on the upstream side. It decreases drastically across the throat of the stenosis, reaches its minimum at the throat, then recovers to 20 mmHg, the specified downstream pressure. Minimum pressure decreases as the prescribed inlet pressure increases, reaches its lowest value (−12.5 mmHg) when inlet pressure reaches its maximum 150 mmHg, then recovers to about 2.5 mmHg, corresponding to minimum inlet pressure 90 mmHg. While the minimum pressure occurs at the throat, the tube wall does not collapse there because the thick-wall stenosis is very stiff.

5.4. Maximum velocity and flow recirculation

Fig. 8 gives plots of the maximum axial velocity as a function of time and the axial velocity profiles at several horizontal cross-sections of the tube with $S_0 = 80\%$ at $t = 0.5$ s when $p_{in} = 150$ mmHg, $p_{out} = 20$ mmHg. Different scales are used for the profiles at different locations to show details of the flow field. The recirculation region and the flow in the negative axial direction are clearly visible.

5.5. Maximum shear stress

Shear stresses at the tube wall corresponding to maximum and minimum inlet pressure are plotted in Fig. 9 for severity $S_0 = 80\%$ with inlet pressure $p_{in} = 150$, 90 mmHg and outlet pressure $p_{out} = 20$ mmHg. The peak shear stress reaches 3270 (dyn/cm^2) which may cause damage to the vessel wall and platelet activation [28].

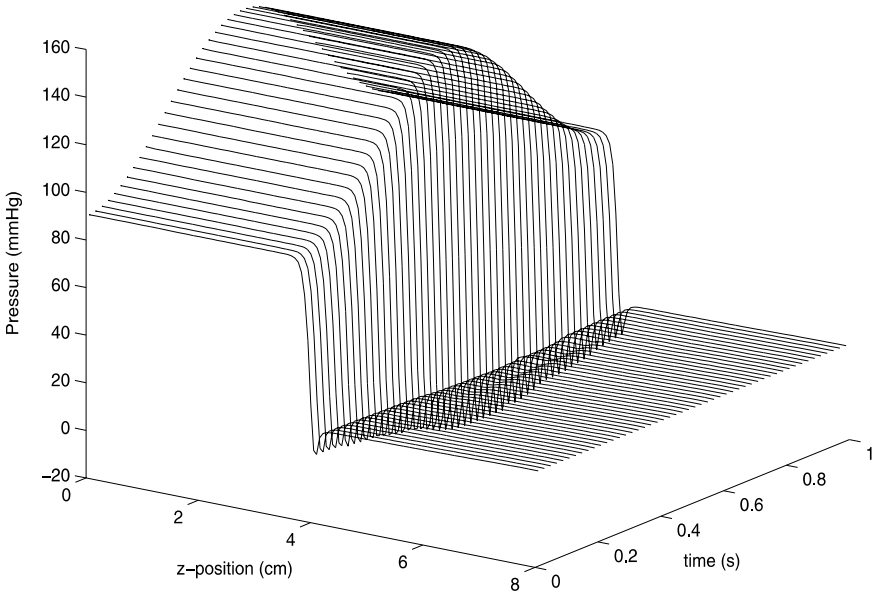

Fig. 7. Transmural pressure along the tube wall $p(z, \theta = 90°, t)$. $p_{in} = 90$–150 mmHg, $p_{out} = 20$ mmHg, $S_0 = 80\%$.

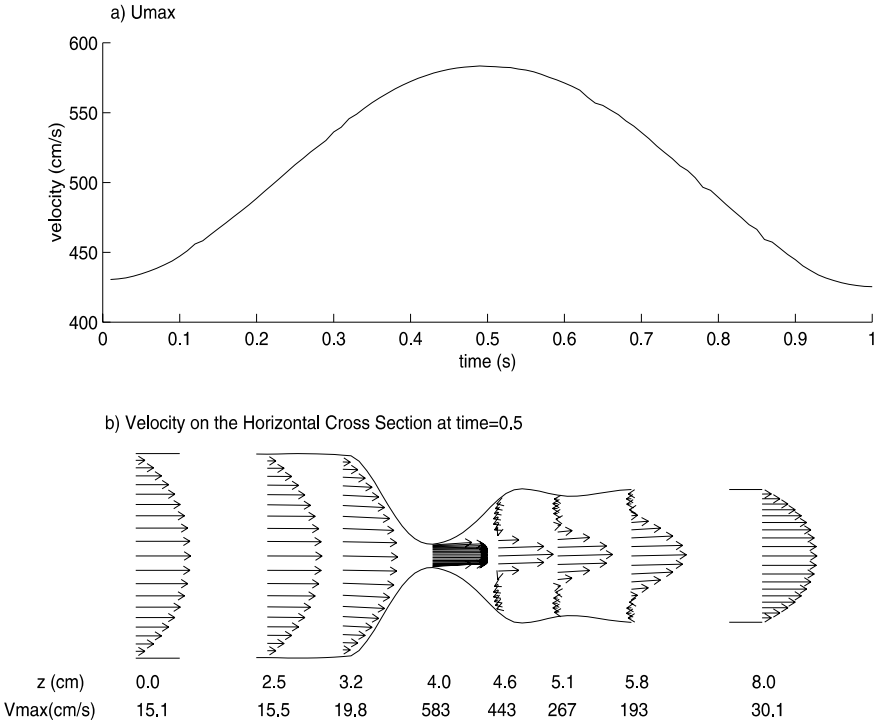

Fig. 8. Behavior of velocity under unsteady pressure and across the stenosis. (a) Maximum axial velocity occurs at the throat of stenosis (centerline) and changes with in-let pressure accordingly; (b) velocity profiles at different axial positions, horizontal cross-section. Different scales are used at different z-locations to show details. $p_{in} = 90$–150 mmHg, $p_{out} = 20$ mmHg, $S_0 = 80\%$.

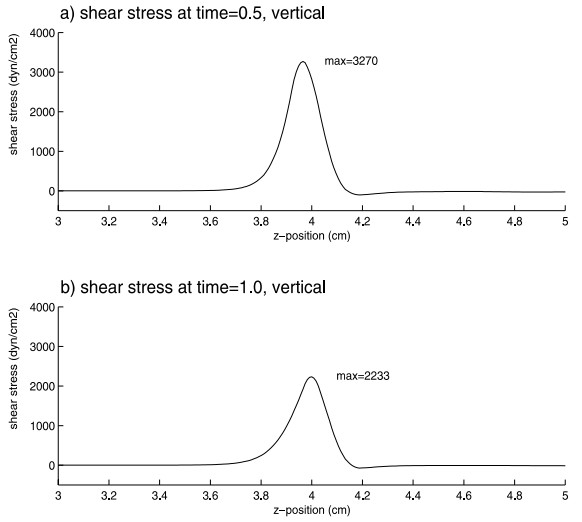

Fig. 9. Shear stress distribution along $\theta = 90°$ line under maximum and minimum inlet pressure.

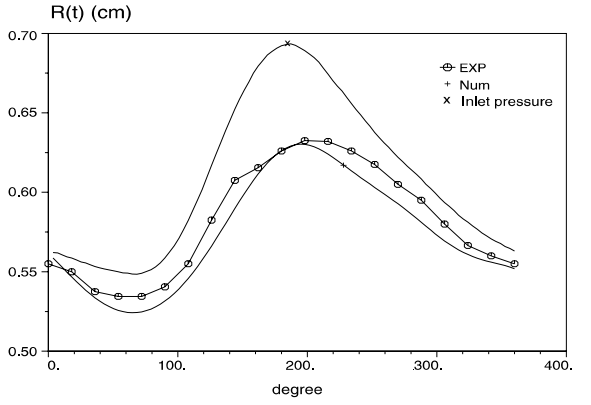

Fig. 10. Comparison of tube radius between numerical and experimental results at cross-section $z = 2.0$ cm. $S_0 = 80\%$, $p_{in} = 70$–130 mmHg, $p_{out} = 60$–80 mmHg.

5.6. Comparison between numerical and experimental results

Fig. 10 plots computational and experimental tube radius variations under pulsatile pressure conditions. The inlet pressure was set to 70–130 mmHg, and outlet pressure was set to 60–80 mmHg (average 70 mmHg) in the experiment. The radius was measured at $z = 2$ cm. The curves show that there is a reasonable agreement between computational and experimental results.

Fig. 11 compares computational and experimental flow rates under unsteady conditions. Pressure conditions imposed at the inlet and outlet of the tube in the

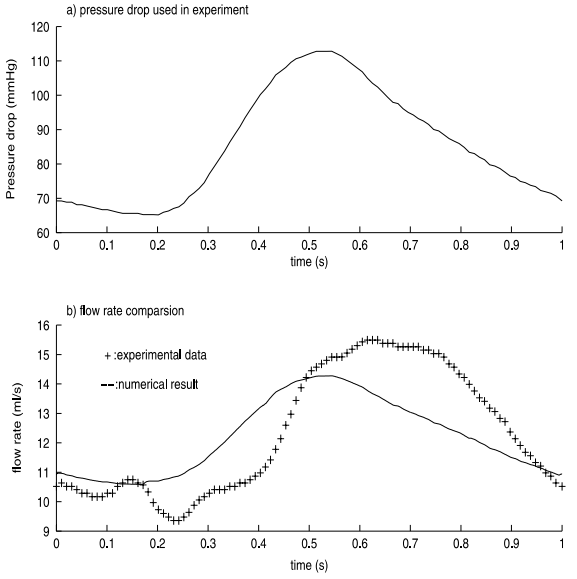

Fig. 11. Comparison of flow rates between numerical and experimental results: flow rate (a) pressure drop curve; (b) flow rate curves. $S_0 = 80\%$, $p_{in} = 70$–130 mmHg, $p_{out\text{-}avg} = 10$ mmHg (0–20 mmHg).

experiment are 70–130 mmHg and 0–20 mmHg (average 10 mmHg) respectively. The outlet pressure was changing slightly because it was not possible to keep it constant in the experiment. Fig. 11(a) plots the pressure drop which is more relevant to flow rate changes. Fig. 11(b) gives the computational and experimental flow rates at the outlet. While there is a rough agreement, we notice that there is a clear phase shift between the computational and experimental data. There is also a phase shift between the experimental flow rate and the imposed pressure condition. A smaller phase shift of tube radius between experimental and numerical data can also be seen in Fig. 10. This may be an indication of viscoelasticity of the tube. A viscoelastic model is currently being developed to improve the elastic model [42]. The wall mechanical properties will also need to be measured under unsteady flow conditions.

Fig. 12 shows pressure–area relationship (tube law) calculated numerically under "no flow" conditions and compared with experimental data. The agreement is good for $p > 0$, remains reasonable for $p > -20$ mmHg, and becomes poor for $p < -20$ mmHg. This indicates that the wall model provides reasonable approximation when tube collapse is minor. The approximation becomes less accurate as tube collapse becomes more severe and caution must be taken when interpreting the numerical results.

6. Discussion

6.1. Comparison with previous computational models

A review of the previous numerical results from 1D models can be found from Downing and Ku [9]. Since the 1D models used only average pressure and axial velocity, the complex pressure distribution near stenosis, axial and radial wall deformation, flow separation and

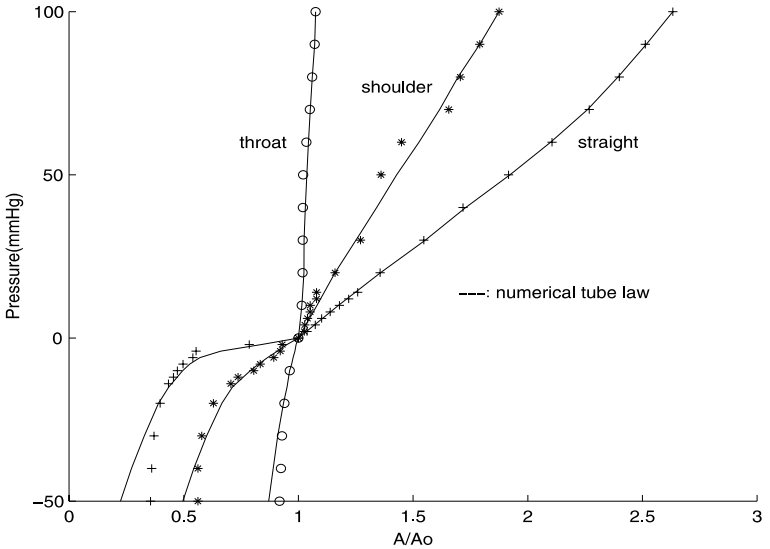

Fig. 12. Comparison of numerical pressure–area relationship (tube law) with experimental data. Calculations were conducted under no-flow condition with $p_{in} = p_{out} = -50$–100 mmHg, $S_0 = 80\%$.

Table 3
Comparison of critical flow characteristics and wall deformation from three stenosis models showing severe stenosis has considerable effects on wall compression and flow behavior

	3D 80% stenosis (current model)	2D 80% attached stenosis [3]	3D 78% stenosis [43]
Tube radius (cm)	0.4	0.2	0.4
Wall thickness (cm)	0.1	0.016	0.1
Axial stretch	36.5%	50%	2%
Radial expansion (under 100 mmHg, with stretch)	60%	22%	12%
p_{in} (mmHg)	90–150	80–120	100 (steady)
p_{out} (mmHg)	20	20 (min)	20
u_{max} (cm/s)	583.5	650	594
Re at inlet	325	197	315
p_{min} (mmHg)	−12.5 (at wall)	−39 (centerline)	−52.5 (at wall)
τ_{max} (dyn/cm^2)	2233–3270 (throat)	7740	3127
Radius reduction	−0.22 (distal)	−0.007 (throat)	−0.002 (throat)
Cyclic tube collapse	Yes	Unable to simulate	Unable to simulate

shear stress information could not be obtained. Existing 2D and 3D models [43,45,46] were limited by the way tube law was implemented: tube cross-section area reduction under collapsed conditions was incorrectly implemented as tube radius reduction in their derivation of the stress–strain relationship for the tube wall. Since tube geometry is one of the most important factors affecting flow and wall behaviors, and the thin-shell theory provides a better interpretation of the tube law under both expansion and collapsed conditions, this new 3D model provides more accurate information about wall deformation and collapse, shear stresses, flow velocity and pressure fields, and gives more accurate predictions about collapse conditions. Comparison of the main results of three models is given by Table 3.

Because of the thin-wall assumption in the model, it was not possible to obtain detailed stress–strain distributions in the tube wall. Tube compressive stress can only be inferred from wall compression and collapse from this model, not direct stress calculation. A thick-wall FSI model is being developed to improve on this model. Results from the thin-wall model can be used as initial approximations.

Phase delays between imposed pressure and wall deformation and flow rates were noticed in the experimental data which may be caused by viscoelasticity of the tube wall. The extend of the viscoelastic effects needs to be investigated by a viscoelastic model. Some preliminary results have been obtained in this regard [42] and we are currently working on a 3D viscoelastic model.

6.2. Physiological significance of the findings

Arteries are made to sustain positive pressure and expansions. Compressive stress and cyclic wall bending and compression may be important in the development of atherosclerotic plaque fracture and subsequent thrombosis or distal embolization. Negative flow pressure is found in the stenotic region which is closely related to compressive stress in the tube wall. In fact, maximum compressive stress is found in the plaque near the throat of the stenosis using a thick-wall model [43]. High shear stress in the order of 2000–3000 dyn/cm^2 at the stenosis may cause damage to the endothelial layer of the vessel wall and platelet aggregation [28]. The flow recirculation region provides an environment with small and alternating shear stresses and prolonged cell residence time favorable for cell adhesion and thrombus formation [6,36]. It was also noticed both experimentally and computationally that if the upstream pressure was high enough and downstream pressure low enough, the tube may collapse and remain collapsed even when upstream pressure drops again. This means the flow would remain choked (actually, fluttering will occur) and the patient may have noticeable clinical symptoms.

6.3. Effect of stenosis severity and pressure conditions

Since pressure decreases considerably when passing a severe stenosis, the effect of the stenosis severity on flow and pressure fields become much more noticeable when comparison is made with comparable flow rates. An 80% stenosis and a 50% stenosis are compared with p_{in} set to 120 ± 30 mmHg for both stenoses, p_{out} set to 20 mmHg for the 80% stenosis and 117 ± 30 mmHg for the 50% stenosis respectively. The average flow rate is 11.0331 ml/s for the 80% stenosis and 11.0354 ml/s for the 50% stenosis. Comparison of the two cases is given in Table 4. While minimum pressure (−12.5 mmHg) and wall collapse were observed for the 80% stenosis, pressure decreased less than 2 mmHg when passing the 50% stenosis and no negative pressure and wall compression

Table 4
Comparison of wall stress and critical flow characteristics from two stenoses under two pressure conditions showing (a) severe stenosis has considerable effects on wall compression and flow behaviors; (b) high pressure causes more critical flow conditions related arterial diseases

	Case 1 (high pressure)	Case 2 (mild stenosis)	Case 3 (normal pressure)
Stenosis severity	80%	50%	80%
p_{in} (mmHg)	90–150	90–150	70–110
p_{out} (mmHg)	20	87–147	20
u_{max} (cm/s)	583.5	104.8	486.1
p_{min} (mmHg)	−12.5	85.4–144.3	−0.41
τ_{max} (dyn/cm^2)	3270	149.4	2522
Hc_{min}	−0.22	0.000186	−0.0025

were observed. Maximum velocity and shear stress for 80% stenosis are 583.5 cm/s and 3270 dyn/cm^2, enough to be of physiological significance, while they are only 104.8 cm/s and 149.4 dyn/cm^2 respectively for the 50% stenosis which do not cause any clinical symptoms. These results are consistent with clinical observations [16].

To see the influence of imposed pulsatile pressure on the flow and wall behaviors, p_{in} was set to 120 ± 30 mmHg and 90 ± 20 mmHg, representing high and normal pressures. p_{out} is set to 20 mmHg. Stenosis severity is still 80% by diameter. While high velocity and high shear stress are observed for both cases, cyclic wall compression and collapse are observed only for the high pressure case. Comparison of the two cases is also included in Table 4. More in vivo experimental validations are needed before these results can become applicable in clinic applications.

7. Conclusion

An experiment-based 3D computational model with FSI was introduced and solved using a GFD method to simulate blood flow in stenotic collapsible carotid arteries. Cyclic wall compression and collapse were observed under physiological pressure conditions. Stenosis severity and pressure conditions are found to be the dominating factors affecting wall compression and collapse and related flow conditions. The unstructured nature of the GFD method made 3D mesh generation and code development possible without much complications. The incremental boundary iteration technique used in this paper can be applied to a wide range of problems with FSI involving large deformations. Critical flow conditions such as negative transmural pressure, high shear stress and large wall deformation caused by severe stenosis under physiological pressure conditions were quantified which may be directly related to artery collapse and plaque cap rupture. Further investigations using viscoelastic 3D thick-wall models are needed to fully simulate the collapse process and make more accurate physiologically-relevant predictions.

Acknowledgements

This research was supported in part by a grant from the Whitaker Foundation and NSF grant DMS-0072873.

References

[1] Aoki T, Ku DN. Collapse of diseases arteries with eccentric cross-section. J Biomech Eng 1993;26(2):133–42.
[2] Bathe KJ. Finite element procedures. Prentice Hall 1996.
[3] Bathe M, Kamm RD. A fluid–structure interaction finite element analysis of pulsatile blood flow through a compliant stenotic artery. J Biomech Eng 1999;121:361–9.
[4] Biz S. Flow in collapsible stenoses: an experimental study. M.S. Thesis, Georgia Institute of Technology, 1993.
[5] Burke AP, Farb A, Malcom GT, Liang YH, Smialek JE, Virmani R. Plaque rupture and sudden death related to exertion in men with coronary artery disease. JAMA 1999;281(10):921–6.
[6] Cao J, Rittgers SE. Particle motion within in vitro models of stenosel internal carotid and left anterior descending coronary arteries. Ann Biomed Eng 1998;26(2):190–9.
[7] Constantinides PA. Plaque hemorrhages their genesis and their role in supra-plaque thrombosis and atherogenesis. In: Pathobiology of the human atherosclerotic plaque. New York: Springer-Verlag; 1990. p. 393–411.
[8] Davies MJ, Thomas AC. Plaque fissuring-the cause of acute myocardial infarction, sudden ischemic death, and crecendo angina. Brit Heart J 1985;53:363–73.
[9] Downing JM, Ku DN. Effects of frictional losses and pulsatile flow on the collapse of stenotic arteries. J Biomech Eng 1997;119:317–24.
[10] Flaherty JE, Keller JB, Rubinow SI. Post buckling behavior of elastic tubes and rings with opposite in contact. SIAM J Appl Math 1972;23:446–55.
[11] Friedman MH. Arteriosclerosis research using vascular flow models: from 2D branches to compliant replicas. J Biomech Eng 1993;115:595–601.

[12] Fung YC. Biodynamics, circulation. New York: Springer-Verlag; 1984.
[13] Fung YC. In: Biomechanics, mechanical properties of living tissues. 2nd ed. New York: Springer-Verlag; 1993.
[14] Fung YC, Liu SQ. Determination of the mechanical properties of the different layers of blood vessels in vivo. Proc Natl Acad Sci USA 1995;92:2169–73.
[15] Fuster V, Stein B, Ambrose JA, Badimon L, Badimon JJ, Chesebro JH. Atherosclerotic plaque rupture and thrombosis. Circulation, Supplement II 1990;82(3):II-47–59.
[16] Giddens DP, Zarins CK, Glagov S. The role of fluid mechanics in the localization and detection of atherosclerosis. J Biomech Eng 1993;115:588–94.
[17] Hafner CD. Minimizing the risks of carotid endarterectomy. J Vasc Surg 1984:392–7.
[18] Hayashi K. Experimental approaches on measuring the mechanical properties and constitutive laws of arterial walls. J Biomech Eng 1993;115:481–8.
[19] Hughes T, Liu WK. Zimmermann, Lagrangian–Eulerian finite element formulation for incompressible viscous flows. Comput Meth Appl Mech Eng 1981;29:329–49.
[20] Judd RM, Mates ME. Flow through a stenosis in a compliant tube. In: Liepsch D, editor. Proc Second Intl Symp on Biofluid Mechanics and Biorheology, Munich, Germany, 1989. p. 417–23.
[21] Kamm RD, Shapiro AH. Unsteady flow in a collapsible tube subjected to external pressure or body force. J Fluid Mech 1979;95:1–78.
[22] Kleiber M. Handbook of computational solid mechanics. New York: Springer-Verlag; 1998.
[23] Kobayashi S, Mijovic B, Tang D, Ku DN. Collapse in high-grade stenosis during pulsatile flow experiments. In: Proceedings of the Third World Congress of Biomechanics, 1998. p. 11.
[24] Kobayashi S, Tang D, Ku DN. Pulsatile flow through a stenotic collapsible tube. In: Proc of the 76th JSME Fall Annu Meeting, 1998. p. 265–6.
[25] Ku DN. Blood flow in arteries. Annu Rev Fluid Mech 1997;29:399–434.
[26] Ku DN, Kobayashi S, Wootton DM, Tang D. Compression from dynamic pressure conditions in models of arterial disease. Ann Biomed Eng 1997;25(supp. 1):S-22.
[27] Ku DN, Zeigler MN, Downing JM. One-dimensional steady inviscid flow through a stenotic collapsible tube. J Biomech Eng 1990;112:444–50.
[28] Lee RT, Richardson SG, Loree HM, et al. Prediction of mechanical properties of human atherosclerotic tissue by high-frequency intravascular ultrasound imaging. Arteriosclerosis 1992:1–5.
[29] Liszka T, Orkisz J. The finite difference method at arbitrary irregular grids and its application in applied mechanics. Comput Struct 1980;11:83–95.
[30] McCord BM, Ku DN. Mechanical rupture of the atherosclerostic plaque fibrous cap. In: Proceedings of 1993 Bioengineering Conference, BED-vol. 24. 1993. p. 324–7.
[31] Patankar SV. Numerical heat transfer and fluid flow. New York: Taylor & Francis Publishers; 1980.
[32] Kamm RD, Pedley TJ. Flow in collapsible tubes: a brief review. J Biomech Eng 1989;111:177–9.
[33] Peskin CS. Mathematical aspects of heart physiology. Lecture notes of Courant Institute of Mathematical Sciences, New York 1975.
[34] Powell BE. Experimental measurements of flow through stenotic collapsible tubes. M.S. Thesis, Georgia Institute of Technology, 1991.
[35] Ramaswamy B, Kawahara M. Arbitrary Lagrangian–Eulerian finite element method for unsteady, convective, incompressible viscous free surface fluid flow. Int J Numer Meth Fluids 1997;7:1053–75.
[36] Rittgers SE, Yu YH, Strony JT. Thrombus formation in moderate coronary stenosis using 2D-LDA. In: Proceedings of the Third World Congress of Biomechanics, 1998. p. 201.
[37] Rugonyi S, Bathe KJ. On finite element analysis of fluid flows fully coupled with structural interactions. CMES 2001;2(2):195–212.
[38] Shapiro AH. Steady flow in collapsible tubes. J Biomech Eng 1977;99:126–47.
[39] Siebes M, Campbell CS, D'Argenio DZ. Fluid dynamics of a partially collapsible stenosis in a flow model of the coronary circulation. J Biomech Eng 1996;118:489–97.
[40] Simon BR, Kaufmann MV, McAfee MA, Baldwin AL. Finite element models for arterial wall mechanics. J Biomech Eng 1993;115:489–96.
[41] Stergiopulos N, Moore Jr JE, Strassle A, Ku DN, Meister JJ. Steady flow test and demonstration of collapse on models of compliant axisymmetric stenoses. Adv Bioeng 1993;ASME BED-26:455–8.
[42] Tang D, Chen XK, Yang C, Kobayashi S, Ku DN. Effects of dynamic wall properties on blood flow in stenotic arteries. J Med Biomech 2000;15(2):77.
[43] Tang D, Yang C, Huang Y, Ku DN. Wall stress and strain analysis using a 3D thick-wall model with fluid–structure interactions for blood flow in carotid arteries with stenoses. Comput Struct 1999;72:341–56.
[44] Tang D, Yang C, Kobayashi S, Ku DN. Steady flow and wall compression in stenotic arteries: a 3D thick-wall model with fluid–wall interactions. J Biomech Eng 2001; 123:548–57.
[45] Tang D, Yang C, Ku DN. A 3D thin-wall model with flow–structure interactions for blood flow in carotid arteries with symmetric and asymmetric stenoses. Comput Struct 1999;72:357–77.
[46] Tang D, Yang J, Yang C, Ku DN. A nonlinear axisymmetric model with fluid–wall interactions for viscous flows in stenotic elastic tubes. J Biomech Eng 1999;121:494–501.
[47] Wootton DM, Ku DN. Fluid mechanics of vascular systems, diseases, and thrombosis. Annu Rev Biomed Eng 1999;1:299–329.
[48] Yamaguchi T, Nakayama T, Kobayashi T. Computations of the wall mechanical response under unsteady flows in arterial diseases. Adv Bioeng 1996;BED-33: 369–70.